and (x_i, y_i) the position of the pixel i. The graphs are shown in the *Inset* of Fig 2*C*. As expected in the pure diffusive case, the mass variance follows the linear law $\sigma_M^2 = 2D_{\text{fluo}}t$. Case ii) displays a very similar scaling. Whereas in case iii) where both cells and food are present, after an initial transition time, σ_M^2 exhibits superdiffusive growth $\sigma_M^2 \sim t^\alpha$ with $\alpha > 1$ for over a decade in time, until the dye blob reaches the chamber boundaries at $t \approx 200$ s. The ratio of characteristic spreading lengths σ_M between tests i) and iii) reaches a maximum of ~6. These results demonstrate how just a few dozen *S. lemnae* can generate chaotic flows that powerfully spread and mix any dissolved or suspended substances, even within the constraints of Stokes flow. One can extrapolate this observation to natural situations where potentially much larger clusters composed of many more individuals form.

3. Hydrodynamic Disturbances Produced by a Single *S.lemnae* Either Fast Crawling or Anchored

3.1. Experimental Measurements. How does a collective flow emerge and how does it relate to the switch in locomotion behavior pointed out in an earlier section? Answering this question requires one to experimentally examine the hydrodynamic disturbances produced by a single cell. We measure and compare the flow in the cell vicinity during the two main locomotion behaviors described previously, i.e. either fast crawling ($v_c \gg 0$) or anchored ($v_c \approx 0$) on a no-slip boundary. In the observation chamber, we inject water containing microbeads that are used as passive tracers to visualize the flow. Since we are ultimately interested in fluid transport and mixing, we use PTV which, unlike Eulerian approaches, provides the essential information about net fluid displacement (*SI Appendix*, section 6A).

The recorded trajectories of microtracers affected by the motion of three fast crawling cells (Movie S9), with crawling speeds around $v_c \approx$ 1,000 to 1,500 μm/s, are gathered and shown in Fig. 3*A* in a single cell frame (see *SI Appendix*, section 6B for the transformation from the lab frame to the cell frame). The tracers move over a persistence time of about $T_p = 0.5$ s. We define the persistence time T_p as the time during which tracers move due to the cell's hydrodynamic perturbation $\boldsymbol{v}(\boldsymbol{x})$ (i.e. above the Brownian motion due to thermal agitation) which for large v_c varies as $T_p \sim 1/v_c$. Microtracers ahead of the cell are first pumped toward the buccal apparatus before being dragged back in the cell's wake as it crawls past the tracers. The general pattern of tracer trajectories reveals a very short-range flow, with those on both lateral sides of the cell resembling the closed loops described by ref. 42, who modeled fluid particle displacement by squirmers. For such trajectories, the net displacement of tracers mostly cancels. A significant net displacement $\Delta x \sim L_c$ can only be found for the tracers located on the cell's path, i.e., for the ones coming into close contact with the stagnation points near the cell body. Indeed, a moving cell can bring in its wake some fluid over even longer distances ("Darwin drift"), though this is typically limited to a very small volume (Movie S10). On the other hand, we measure the feeding flow produced by an anchored cell (*SI Appendix*, section 6C and Movie S11), an example of which is displayed in Fig. 3*B*. In this example, lasting $T_p = 7.6$ s, the flow is unidirectional, and the net tracer displacement reaches distances up to 5 to $6L_c$. We can qualitatively see from the direct comparison between the two cases that the long-range feeding flow is considerably more efficient at transporting fluid over long distances, and this is all the more true as the cell remains motionless and feeds. While feeding, *S. lemnae* remains motionless on average for a few seconds and may reach pumping times of ~100 s.

3.2. Modeling the Individual Feeding Flow by a Regularized Stokeslet above a No-Slip Plane. We model the single feeding flow by a regularized (volume) Stokeslet above a wall, from the theory developed by refs. 41 and 43 (*SI Appendix*, section 6D). The model needs five parameters: the location of the force $\boldsymbol{x}_f$ in the xy plane, its height h above the wall, the radius of the force δ, the 3D orientation of the force $\boldsymbol{F}_p/|\boldsymbol{F}_p| = (\cos\theta\cos\phi, \sin\theta\cos\phi, \sin\phi)$ (where θ and ϕ are, respectively, the angle with respect to the x axis in the xy plane and the angle with respect to the wall $z = 0$) and its magnitude $F_p = |\boldsymbol{F}_p|$. The parameters $\boldsymbol{x}_f$, h, δ and ϕ are fixed and extracted from the anatomical features of *S. lemnae* (see the scheme of Fig. 1*B*). The force is located at $\boldsymbol{x}_f = \boldsymbol{x}_c - (L_c/2)\boldsymbol{F}_p^{xy}/|\boldsymbol{F}_p|$, where $\boldsymbol{x}_c$ is the cell center, L_c its average length, and $\boldsymbol{F}_p^{xy}/|\boldsymbol{F}_p| = (\cos\theta, \sin\theta)$ the force orientation in the xy plane. The parameter h is the height of the cell's anterior above the plane and the force radius δ is taken as the cell's half-width. The angle ϕ with respect to the $z = 0$ wall is measured from the systematic inclination of the cell's anterior toward the top. In summary, we measure on average $L_c \approx 200$ μm, $h \approx 50$ μm, $\delta \approx 43$ μm, and $\phi \approx 13°$. These values are held constant across all cells, ignoring the slight variation in their size. Only the cell position $\boldsymbol{x}_c$ and orientation θ vary and will be extracted systematically from images. In Fig. 3*C*, analytical streamlines are compared to a set of experimental streamlines consisting in nine individual feeding flows superimposed all together, produced by nine different cells of slightly varying size, with $Lc = 200 \pm 20$ μm (*SI Appendix*, section 6C–E). Visual comparison between analytical and experimental streamlines shows a nearly perfect geometrical match, thus validating the model. Note that the flow is inherently 3D, as the wall imparts parallel shear and bending of the streamlines in the transverse z-direction (*SI Appendix*, Fig. S5*A*). Last, the force magnitude $|\boldsymbol{F}_p|$ is obtained by least-squares fitting of analytical and experimental velocity magnitudes, yielding $|\boldsymbol{F}_p| = 1{,}200 \pm 240$pN (*SI Appendix*, section 6E). This value is consistent with reported force magnitudes for other attached filter feeders when plotted as a function of cell dimension; see *SI Appendix*, Fig. S6. The main source of error in estimating $|\boldsymbol{F}_p|$ stems from the slight variability in cell size L_c, and we expect it to be the main source of error for computing the total collective flow as well. These velocity field measurements allow us to estimate both Reynolds and Péclet numbers. The Reynolds number is $Re = vL/\nu$, with L the characteristic feeding flow size, v the fluid velocity and $\nu \approx 10^{-6}$ m^2/s the kinematic viscosity of water. Taking $L = 500 \times 10^{-6}$ m and $v = 100 \times 10^{-6}$ m/s, we get $Re = 0.05 \ll 1$, ensuring Stokes conditions. The Péclet number for the fluorescein experiment shown in Fig. 2 is estimated as $\text{Pe}_{\text{active}} = vL/D_{\text{fluo}} \approx 125$, and for oxygen, $\text{Pe}_{\text{active}} \approx 25$. Given the reported diffusivity of dissolved organic matter ranging from $D = 10^{-12}$ to 10^{-9} m^2/s (44), the corresponding Pe_{active} spans 50 to 50,000, giving a first hint of the dominance of feeding flows over diffusion for many nutrients.

3.3. The Locomotion Speed Determines the Type of Hydrodynamic Disturbance. We explain the origin of the two hydrodynamic disturbances using the balance of forces applied to the cell while crawling at a given speed v_c (see scheme of Fig. 1*B*). The drag force $\boldsymbol{F}_d$ opposes two propulsive forces, i.e. the pumping force $\boldsymbol{F}_p$ generated by its AZM and the contact

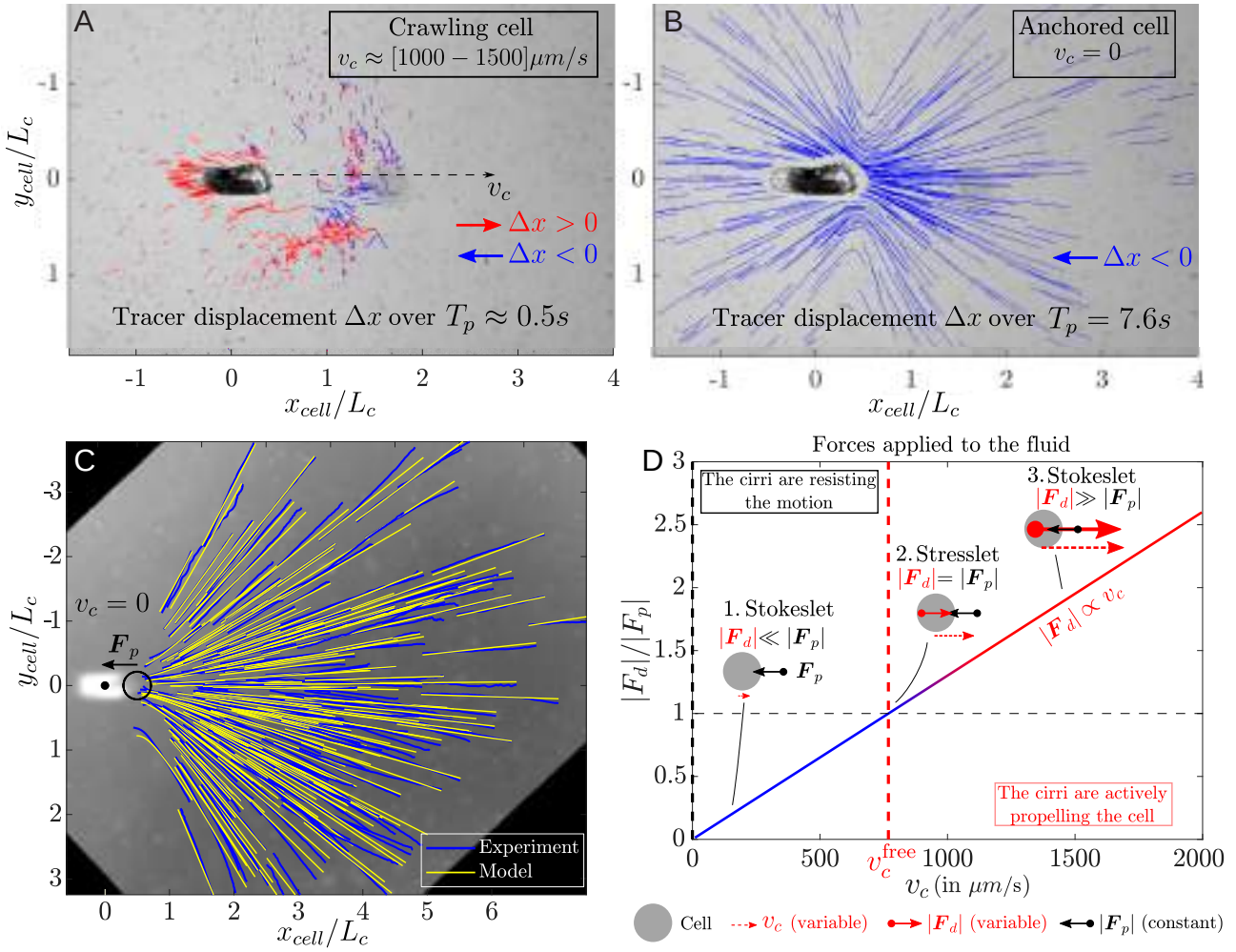

Fig. 3. Comparison of the hydrodynamic disturbances caused by an isolated *S. lemnae* either (*A*) crawling ($v_c \gg 0$) or (*B*) immobile ($v_c \approx 0$), projected in the *xy* plane, in the cell frame. In the crawling case (*A*), fluid particles are displaced over a persistence time about $T_p \approx 0.5$ s. In the immobile case (*B*), the cell remains anchored for $T_p = 7.6$ s. In both cases, fluid particles trajectories are colored blue if they move left ($\Delta x < 0$) or red if they move right ($\Delta x > 0$). (*C*) Comparison between the experimentally measured streamlines (in blue) ahead of a feeding cell and the theoretical streamlines predicted by the model of ref. 41 (in yellow), in the *xy* plane. The black dot marks the center of the ellipsoid matching the cell's body $\boldsymbol{x}_c = (0, 0)$, and the black circle indicates the position $\boldsymbol{x}_f$ and radius δ of the volume force. (*D*) Relative importance of the magnitude of the two opposite forces applied to the fluid by the action of the cell (depicted as a gray disk), i.e. drag force F_d vs. pumping force F_p. F_p is assumed to be constant, while F_d scales as $F_d \propto v_c$. Depending on the ratio F_d/F_p, three distinct scenarios for the far-flows are identified: 1) Immobile or slow-moving Stokeslet above a wall, with $\boldsymbol{F}_p$ opposite to the cell's motion. 2) Stresslet above a wall, at the terminal velocity $v_c^{\text{free}} \approx 770\,\mu$m/s. 3) Fast-moving Stokeslet $\boldsymbol{F}_d$ aligned with the cell's motion.

force $\boldsymbol{F}_c$ between the cirri and the solid substrate. Hence, for a cell crawling in a straight line at constant speed, we have the balance of forces $\boldsymbol{F}_d = -(\boldsymbol{F}_c + \boldsymbol{F}_p)$. Since drag is proportional to speed $\boldsymbol{F}_d = -C_d \boldsymbol{v_c}$ (with C_d the drag coefficient whose value is estimated in *SI Appendix*, section 7), the cell speed $\boldsymbol{v_c}$ is given by

$$\boldsymbol{v_c} = \frac{1}{C_d}(\boldsymbol{F}_c + \boldsymbol{F}_p). \qquad [1]$$

In what proportion do these two forces contribute to v_c? Based on observations that the AZM appears to be consistently active during both crawling and pumping, we assume that the pumping force magnitude $|\boldsymbol{F}_p| = 1{,}200$ pN remains constant. Only during brief SSR events or rare mitosis does the AZM seem to stop. In the event that $\boldsymbol{F}_p$ was the only propulsive force and $\boldsymbol{F}_c = 0$, $\boldsymbol{F}_d$ would balance $\boldsymbol{F}_p$ at a terminal speed $v_c \approx 770\,\mu$m/s (see again *SI Appendix*, section 7). Yet, *S. lemnae* can achieve much greater locomotion speed, up to $v_c \sim 7{,}000\,\mu$m/s, as can be seen in Fig. 1*H*, which suggests that the force $\boldsymbol{F}_c$ plays a driving role in the crawling mode.

How do these forces impact the surrounding fluid? While three forces act on the cell, only two forces are exerted by the cell on the fluid, namely the opposite forces $-\boldsymbol{F}_p$ and $-\boldsymbol{F}_d$. In fact, the contact force $\boldsymbol{F}_c$ between the cirri and the wall is assumed to be fully transmitted to the substrate and to have no effect on the fluid. However, $F_c = |\boldsymbol{F}_c|$ as an external force ultimately determines the amount of drag force $F_d = |\boldsymbol{F}_d|$, since $F_d \propto v_c$, and $v_c \propto F_c$ according to Eq. **1**. As a consequence, we end up with three regimes of far-field flows, depending on the relative importance of F_d over the constant F_p, as summarized in Fig. 3*D*. When the cell is immobile ($v_c = 0$; see Fig. 3*B*) or crawling slowly, such that $F_d/F_p \ll 1$, it produces an unaltered pumping flow, approximated as a Stokeslet above a wall, decaying as $v \sim 1/r^2$, and opposite to the cell's motion. When $F_d/F_p = 1$ (i.e. for $v_c^{\text{free}} \approx 770\,\mu$m/s), and neglecting the slight inclination of $\boldsymbol{F}_p$ with respect to $\boldsymbol{F}_d$ as shown in Fig. 1*B*, the far field corresponds to a stresslet (dipole force) above a wall that decays as $v \sim 1/r^3$ (45), producing fluid trajectories close to those shown in Fig. 3*A*. In this specific case, no net force is exerted

on the fluid. Finally, when the cell reaches high speed for which $F_d/F_p \gg 1$, the far field is again a Stokeslet above a wall, but aligned with the cell's motion.

3.4. Either the Cell Moves or it Moves the Fluid. The origin of collective flow lies in the ability of a single hydrodynamic disturbance to displace fluid over distances Δx comparable to separation distances between feeding cells d_c. In fact, the far-field flows pointed out in the previous section induce very different net fluid displacements. The net tracer displacement $\Delta x = |\boldsymbol{x} - \boldsymbol{x_0}|$ is computed by integrating the advection equation $\dot{\boldsymbol{x}} = \boldsymbol{v}(\boldsymbol{x}(t), t)$ from an initial position $\boldsymbol{x_0}$:

$$\Delta x = \left| \int_0^{T_p} \boldsymbol{v}(\boldsymbol{x}(t), t) dt \right| . \qquad [2]$$

Two main factors influence Δx: the nature of the velocity vector field $\boldsymbol{v}(\boldsymbol{x})$ (e.g. whether it is unidirectional and how it decays spatially $v \sim 1/r^n$), and the persistence time T_p. Stokeslets transport fluid more effectively than stresslets, as already clear from the comparison between Fig. 3 *A* and *B*. Then, among the two main scenarios involving Stokeslets (1 and 3 in Fig. 3*D*), the persistence time T_p makes the difference: At constant force magnitude, the total fluid volume moved is the same, but faster-moving cells interact with more particles, displacing each one less on average (*SI Appendix*, section 8). In brief, the feeding flow range is maximum for $v_c = 0$, and any increase in v_c reduces it, both because $F_d \propto v_c$ and $T_p \propto 1/v_c$ (*SI Appendix*, section 8). Thus, the difference in hydrodynamics observed between Fig. 2 *C*, (*ii*), and (*iii*) is explained by the global reduction of v_c triggered by food injection, as observed in earlier section. In short, either the cell moves or it moves the fluid. Then, considering that the feeding cells remain immobile over $\tau_c \approx 2$ s on average (as shown later in Section 5), in such a case, the feeding flow extends up to $\Delta x \sim 2.5 L_c$ in the xy plane. This is comparable to the average separation distance between feeding cells measured in the experiment illustrated in Fig. 2 *A*, (*ii*), which gave $\langle d_c \rangle \sim 4.5 L_c$, so that $\Delta x \sim \langle d_c \rangle/2$, implying that pumping flows interact hydrodynamically (*SI Appendix*, section 9 for the method to measure d_c). In the following collective flow model, we disregard the hydrodynamic contributions of the last two scenarios by setting a maximum locomotion speed threshold $v_c^{\max}$ over which cells are considered to exert no force on the fluid. We select $v_c^{\max} = 500$ µm/s, after noticing that the proportion of feeding cells varies little with the choice of $v_c^{\max}$ between 300 µm/s and 700 µm/s (*SI Appendix*, section 17).

4. Characterization of the Collective Feeding Flow

4.1. Analytical Skin Friction Field on the Solid Boundary. To quantify the strong mixing and dispersion properties of the collective flow observed in Fig. 2, one would ideally need access to the full, time-evolving 3D velocity field. We here overcome this experimental challenge by demonstrating that the flow can be entirely inferred from its salient topological features (46), which stem from stagnation (critical) points of the skin friction field on the wall. To illustrate this concept, we consider a simple case where two cells pump in opposite directions, and predict how the resulting flow organizes the spatial distribution of a cloud of tracers (2 µm microbeads mixed with *Chlorogonium*-free medium) injected nearby (Fig. 4*A* and Movie S12). Given the linearity of the Stokes equation, the total velocity field $\boldsymbol{v}$ at time

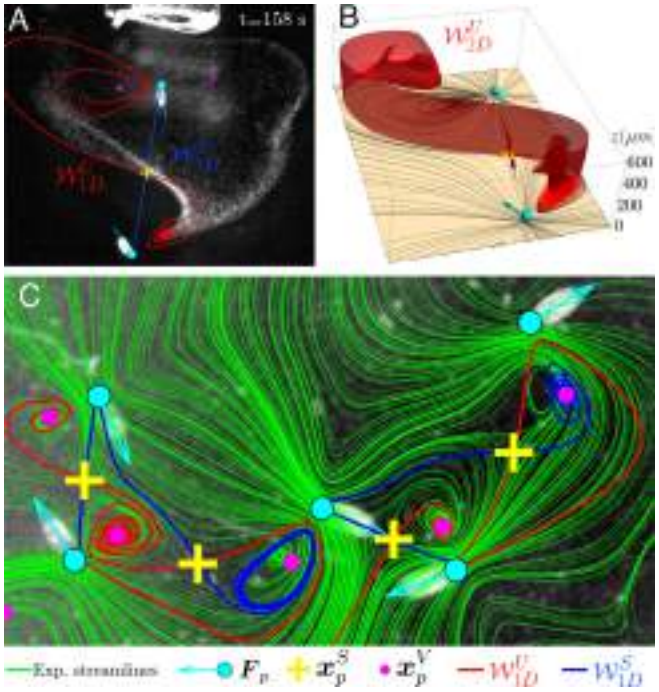

Fig. 4. (*A*) Image of two *S. lemnae* oriented in opposite directions while feeding on a mixture of *Chlorogonium*-free medium and tracer beads (appearing as a cloud of white dots, injected 158 s earlier from the syringe tip visible at the top). Superimposed on the image are the numerical 1D manifolds $\mathcal{W}_{1D}$ emerging from the hyperbolic point $\boldsymbol{x}_p^S$ of the analytical skin friction field, computed by summing the two volume forces (with positions and orientations extracted from the cell images, depicted as cyan dots and arrows respectively). (*B*) Associated 2D manifold $\mathcal{W}_{2D}$ repelled from $\mathcal{W}_{1D}$ of the skin friction field (whose streamlines are displayed as continuous black lines lying on the $z = 0$ plane) generated by the configuration of cells shown in (*A*). (*C*) Instantaneous streamlines (in green) of the experimentally measured velocity field in the $z = 150$ µm plane, produced by a group of feeding cells. Superimposed are the 1D manifolds $\mathcal{W}_{1D}$ from the associated analytical skin friction field. For clarity, $\mathcal{W}_{1D}$ are truncated at intersections with volume forces.

of image t_j and position $\boldsymbol{x} = (x, y, z)$ is simply the sum of all N single pumping flow $\boldsymbol{v}_i(\boldsymbol{x}, t_j)$:

$$\boldsymbol{v}(\boldsymbol{x}, t_j) = \sum_{i=1}^{N} \boldsymbol{v}_i(\boldsymbol{x}, t_j) . \qquad [3]$$

where each $\boldsymbol{v}_i$ depends on the position and orientation of the cell i (provided $v_c < v_c^{\max}$). Similarly, the skin friction field on the wall $z = 0$, defined as $\boldsymbol{\tau}_i(x, y) = \partial \boldsymbol{v}_i/\partial z|_{z=0}$, is also additive, so that the total skin friction is $\boldsymbol{\tau}(t_j) = \sum_{i=1}^{N} \boldsymbol{\tau}_i(t_j)$. In the example of Fig. 4*A*, since the two cells are pumping in opposite directions, a stagnation point must lie on the wall between them, meaning that the skin friction field cancels at a critical point $\boldsymbol{x}_p$, defined as $\boldsymbol{\tau}(\boldsymbol{x}_p) = 0$. This critical point is found to be a saddle point $\boldsymbol{x}_p^S$ (*SI Appendix*, section 10B). Surana et al. (47) demonstrate that saddle points of the skin friction field are the starting/ending points of 2D manifolds $\mathcal{W}_{2D}$, which act as separation/reattachment material surfaces that propagate in the fluid interior. The 2D stable/unstable manifolds are computed numerically by advecting backward/forward in time some tracer particles initially placed just above the detected separation/reattachment critical skin friction lines (see example of $\mathcal{W}_{2D}$ of Fig. 4*B*, coming from $\mathcal{W}_{1D}^S$ of Fig. 4*A*). These 2D surfaces are crucial in our system for two reasons: First, they are surfaces with locally minimal flux, thus

forming a flow skeleton (48) that governs fluid transport; second, because they also induce exponential stretching or compression of nearby fluid elements, they coincide with part of the Lagrangian Coherent Structures (LCSs) that control fluid deformation, and ultimately mixing (46). Getting back to our example seen in Fig. 4 *A* and *B*, the influence of the 2D unstable manifold $\mathcal{W}^U_{2D}$ on the spatial distribution of the cloud of tracers is evident: $\mathcal{W}^U_{2D}$ attracts the cloud, which ultimately fits its shape, perfectly in the *Bottom Right* of the image, whereas the syringe tip and an off-frame cell distort the tracers distribution in the *Top Left* corner. Nevertheless, the global match illustrates that 3D tracer dynamics can be predicted from analytical critical skin friction lines alone. Next we check that the experimental flow patterns can be systematically predicted for the many diverse configurations of cell number, relative positions, and orientations encountered through the imaging. It should be noted that, because our flow is said "open" (the flow intensity vanishes in the z direction), the criteria for defining reattachment/separation surfaces (47) are not always strictly fulfilled. Anyway, we show in *SI Appendix*, section 10C that this has little importance as long as we do not look too far from the bottom wall $z = 0$.

4.2. Velocity Field Measurement and Comparison with the Analytical Skin Friction Field. For each image, the collective velocity field within a feeding cell group is measured using Particle Image Velocimetry (PIV) in a focal plane set at $z_{\text{fp}} = 3h$ above the bottom plate. We inject a mixture of water seeded with microbeads and containing just enough *Chlorogonium* cells to spark the feeding behavior in *S. lemnae*. We get the instantaneous flow by computing the streamlines—curves tangent to the velocity vector field—at each time step (*SI Appendix*, section 10A), with examples shown in Fig. 4*C* and *SI Appendix*, Fig. S9 and Movies S13 and S14. Rich flow patterns can be observed, with a mingling of saddle points and vortices forming, bifurcating and breaking over time, as the cells crawl, stop, and reorient. On these experimental streamlines, we overlay critical points and skin friction lines calculated from the same configuration of cell positions and orientations. Although we compare two sets of streamlines that are separated vertically by $z = 3h = 150\,\mu\text{m}$, we assume this gap is small enough so that the sketch drawn by the critical skin friction lines $\mathcal{W}_{1D}$ on the wall is representative of the flow patterns in the measurement plane. Within the resolution limits, and provided no off-frame cell alters the flow within the frame, the agreement between experimental and analytical patterns is remarkable, regardless of cell number, separation distance, or orientation. The minor discrepancies sometimes observed likely stem from the finite-size distribution of cell sizes (and so of the pumping force $|\boldsymbol{F}_p|$), which is not included in our model. We emphasize that our collective flow model is all the more reliable because the feeding force never fluctuated throughout the experiments, even when the cell was fully fed. Further validation of the unsteady collective flow model is provided by comparing tracers advected numerically by the feeding cluster of Movie S6 with the actual evolution of the yeast cloud (Movie S15).

5. Dispersion and Mixing Properties of the Collective Feeding Flow

5.1. Cells Dispersion vs. Fluid Dispersion. To further explore the close relationship between locomotion speed v_c and fluid transport efficiency, we quantify the dispersion dynamics of both cells and simulated fluid particles, from the formation of a feeding cluster to its disbanding. As shown in Fig. 2 *A* and *B*, cells initially wandering around soon form a feeding cluster around the yeast injection point. Eight movies lasting $T \approx 3.5$ min each are grabbed approximately every 15 min after food injection at time t_0, up to $t - t_0 = 109$ min. We assume cell behavior is stationary over the duration of each movie. In Fig. 5*A*, the cell MSD for each movie is plotted as a function of $\tilde{t} \in [0, T]$, where $\tilde{t}$ denotes the time elapsed since the start of that specific movie. Regarding the first movie $t - t_0 = 3$ min, the cell MSD (labeled in purple) tends toward a plateau. This behavior is reminiscent of chemotaxis, as cells adapt their locomotion to remain near the injection point after detecting it, contrasting with the Fickian behavior ($\text{MSD} \sim 4D_{\text{WF}}\tilde{t}$) observed under uniform food conditions, as seen in Section 1. At successive times $t - t_0$ we observe a monotonic growth of the MSDs, which ultimately tend to the faster Fickian regime ($\text{MSD} \sim 4D_{\text{NF}}\tilde{t}$), as accessible food probably becomes scarcer (SD values for the data shown in Fig. 5*A* are provided in *SI Appendix*, section 11).

To compute fluid dispersion, 2,500 material elements (tracers) are initially arranged on a regular grid at $z_0 = 150\,\mu\text{m}$ that covers most of the cluster area (*SI Appendix*, section 12A and Movie S16). The tracers are advected using the collective flow computed from the evolving cell positions and orientations collected from every movie. We compute the MSDs in both the xy plane and z-direction. Note that in our system, the average fluid fluctuations decay with distance z from the surface (50). As some tracers are gradually repelled from the surface, the resulting MSDs in both the xy plane and along z will inevitably decrease, to exhibit a subdiffusive regime. Accordingly, we limit the comparison to relative MSDs, bearing in mind that absolute values depend on integration time. In contrast to cell MSDs, tracer MSDs reveal the opposite temporal dynamics: From time $t - t_0 = 15$ min, a diffusive regime is reached with a maximal dispersion coefficient about $D_{Flxy} = 6.10^{-9}\,\text{m}^2/\text{s}$ (in comparison, at the same time, $D_{Flz} \approx 8.10^{-10}\,\text{m}^2/\text{s} = D_{Flxy}/7.5$; see *SI Appendix*, Fig. S11*B*), before a steady decline of the dispersion coefficient through the successive movies. These opposite spreading dynamics align with previous results, with cell MSDs primarily governed by locomotion speed v_c. The increase in cell MSDs reflects a steady rise in $\langle v_c^2 \rangle$, evident from the evolving velocity distribution (Fig. 5*B*), which gradually shifts from low to high v_c values, i.e. beyond the threshold $v_c^{\max} = 500\,\mu\text{m/s}$, above which cells no longer exert a pumping force in the model. As a result, the fraction of feeding cells (i.e. for which $v_c < v_c^{\max}$) drops from ~90% just after injection to ~65%, on the way back to the 40% measured prior to injection (see the *Inset* of Fig. 5*B*). As time goes by, fewer cells contribute to the collective flow, and the tracer MSD decreases. The opposing trends between cell MSD and tracer MSD reflect the remarkable behavioral flexibility of *S. lemnae*, which employs a dynamic trade-off between chemotaxis and collective flow to swiftly adapt to ephemeral patches of food.

We compare our simulated fluid dispersion for feeding cells, D_{Flxy}, with an estimate of the fluid dispersion that would result solely from crawling cells. Assuming the cells crawl at the constant speed of $v_c^{\text{free}} \approx 770\,\mu\text{m/s}$, their far-field flow can be approximated by a stresslet. In this case, we can use the model by Lin et al. (42) whose estimation of the fluid dispersion coefficient κ for a dilute suspension of moving squirmers is dominated by the stresslet flow induced by each squirmer. Using parameters derived from *S. lemnae*'s geometry and considering the equivalent population density as in the movie $t - t_0 = 15$ min (*SI Appendix*, section 12B for further details), we find $\kappa \approx 2.10^{-10}\,\text{m}^2/\text{s}$